INVITED: Integrated Millimeter-Wave/Terahertz Sensor Systems for Near-Field IoT

Payam Heydari
Nanoscale Communication IC (NCIC) Labs, University of California, Irvine, CA

***Abstract* — The emergence of Internet of Things (IoT) has brought forth new opportunities by seamlessly integrating the physical world using computing, sensing, and wireless networks, transforming it into a cyber-physical system. An essential building block enabling an IoT is a sensing system. The use of "near-field communication (NFC)" has gained attention in recent years, as it enables low-power short-range sensing and wireless transfer of low content information. The NFC, however, is inapplicable in scenarios where the real-time high-resolution image or video of the object(s) needs to be sensed. The penetration of THz waves through many materials, which are impervious for visible light makes THz imaging akin to X-rays, except that THz radiation is non-ionizing and therefore not harmful to the object being imaged, especially living tissues. This special issue paper presents an overview of recent advances in the development of silicon-based mm-wave/THz imaging sensors for near-field IoT applications.**

Keyword* — *Internet-of-Things (IoT), Sensors, Silicon, CMOS, Terahertz (THz), millimeter-wave (mm-wave), receiver, transmitter, imaging, spectroscopy

I. INTRODUCTION

Internet-of-Things (IoT) will arguably be the next wave of information technology revolution. It brings forth seamless machine-to-machine interaction in the physical world using computer, sensing, and wireless networks, transforming it into a cyber-physical system. While the main R&D efforts have, so far, been on the development of more powerful computing and communication devices, the IoT extends the concept of connectivity to literally all physical systems/objects uniquely identified using sensors and/or actuators (Fig. 1).

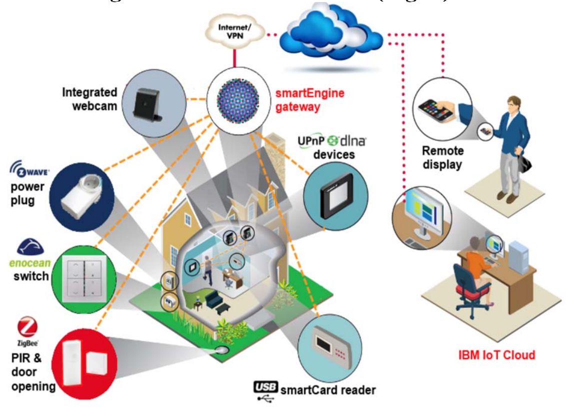

Fig. 1. A general concept of IoT (*courtesy of IBM*) [1].

DAC '16, June 05-09, 2016, Austin, TX, USA
© 2016 ACM. ISBN 978-1-4503-4236-0/16/06…$15.00
DOI: http://dx.doi.org/10.1145/2897937.2907985

The notion of "intelligent" communication between devices within an IoT mandates that they incorporate intelligent sensors that can proactively sense and communicate specific aspects of these devices. The possibility of tagging, tracking, and "identifying" the objects in a cyber-physical system goes hand-in-hand with the deployment of IoT concept. In this context, the NFC-based sensors may play a critical role, as electronic/electrical devices can readily be identified, called, controlled or configured using these sensors. The NFC-based sensors, therefore, facilitate low-power and short-range electronic identification that is suitable for connectivity to an IoT network. Many applications, however, require sensors that are capable of sensing and detecting more sophisticated content than a simple bar-code. For example, sensors needed for food and agriculture industry must be able to detect specific chemical or organic ingredient. The security and surveillance applications require sensors that can see through objects and project the image of hidden objects (e.g., weapons or knives) underneath covers or cloths.

Recently, frequency range from 0.1-3 THz - known as THz gap (Fig. 2(a)) - has enabled disruptive applications such as 10-gigabit-per-second wireless communications as well as active/passive sensing. Many materials that appear opaque in the visible light spectrum are transparent in the THz band and vice versa [2]. One of the key features of THz radiation is its spectral distinctiveness. Typical photon energies of THz radiation are on the order of a few meV. Since many molecules exhibit activation energies for vibrations and rotations, which are also on the order of a few meV, these molecules feature a specific spectroscopic fingerprint in this frequency region, allowing for chemical recognition. Furthermore, THz radiation penetrates through many materials which are impervious for visible light, such as paper, textiles and various plastics. Therefore, THz imaging is akin to X-rays, except that THz radiation is non-ionizing and, therefore, not harmful to the object being imaged, especially living tissues (Fig. 2(b)). This attribute is useful in many applications, including security (weapon detection—simulated THz image of man with a gun hidden underneath his cloth as depicted in Fig. 2(c)), and biological sensing such as skin-cancer detection. In fact, great research effort on the THz sensing of absorption and scattering characteristics of fundamental bio-agents (e.g., DNA) and related biological materials [3]-[5] have been conducted to produce credible experimental evidence for the existence of species-specific *resonance features* that arise from phonon mode activity at the molecular level [5].

Nanoscale silicon process has achieved the required system performance [7-11] that had previously only been obtained using III-V technologies in multi-chip-module-based platforms [12-14]. The availability of silicon-based imaging sensors can be especially advantageous when a large number of array elements is required. Furthermore, the high yield of silicon makes it possible to develop wafer-level imaging array sensors to achieve fast scan-time.

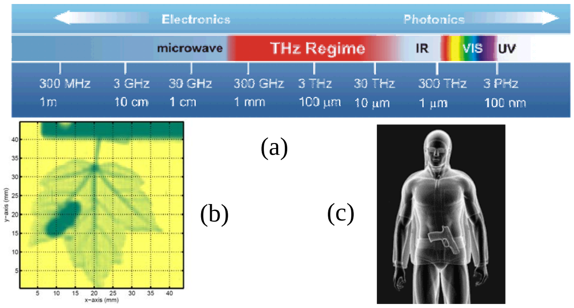

Fig. 2. (a) THz band, (b) imaged obtained from a THz sensor, and (c) through-material image of an individual with hidden gun [6].

This paper provides an overview of the design of high performance silicon-based THz IC's for sensing and imaging. In rationalizing why silicon is one of the best technologies of choice for medium to mass market applications, system-level considerations and circuit design issues are discussed and case studies are presented.

II. System-Level Considerations

From architectural standpoint, imaging systems are categorized into active and passive.

A passive imaging sensor detects black-body radiation from the objects at the room temperature. Normal matters emit electromagnetic radiation when their nominal temperatures are above absolute zero [15]. The radiation represents a conversion of a body's thermal energy into electromagnetic (EM) energy, and is therefore, called thermal radiation. It is a spontaneous process of radiative distribution of entropy. The amount of EM energy that an object reflects or emits is characterized by the emissivity ε of the object, which is a function of its dielectric properties, the roughness of its surface, and the observation angle. At THz frequency range, the spectral radiance B_f (which is a measure of the power emitted to or reflected from a surface, and received by an imaging system looking at that surface) is given by Planck black-body radiation [15]:

$$B_f = \frac{2hf^3}{c^2}\left[1 \Big/ \exp\left(\frac{hf}{kT}\right) - 1\right] \qquad (1)$$

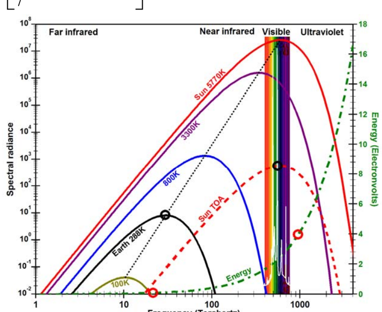

Fig. 3. Spectral radiance vs. frequency. When temperature increases, the spectral radiance will increase for each and every frequency and the peak spectral radiance moves to a higher frequency [16].

where k is the Boltzmann constant, h denotes the Planck constant, c is the speed of light in the medium (whether material or vacuum), f is the frequency, and T is the temperature in K. One can infer that at higher frequencies (up to the brightness peak), the resolution is increased with frequency (Fig. 3). A perfect radiator, known as a black-body, has ε= 1, whereas a perfect reflector has ε= 0. The human body (and the skin tissue) has an emissivity on the order of 0.9. A passive radiometer collects the power naturally radiated from the target object and produces an output voltage proportional to the incident power (Fig. 4(a)).

Active imagers, on the other hand, transmit signal towards the object and use the reflected signal to form the image. One example of an active imaging system is depicted in Fig. 4(b), which is based on optical radiation/detection. This example incorporates a broadband frequency synthesizer and a laser modulator on the transmitter (TX) side, and amplitude/phase detectors and digitizers (i.e., ADC) on the detector side. The signal generator produces frequency-tuned signals with frequency varying across a tuning range (e.g., 10 MHz - 10 GHz). The synthesized signal is split off using a power divider into two signals: (1) a reference template for amplitude and phase detector on the receiver (RX) side, and (2) a modulating signal that modulates the laser intensity. The amplifier in the transmitter must amplify the signal so as to drive the laser diode. The laser diode then beams laser light into the object. After being reflected from the tissue, the laser signal is received by the photo detector, which is converted back into an electrical RF signal. This RF signal is amplified and compared against the reference. The constituent amplitude and phase detectors measure the attenuation and the phase shift of the received signal.

In active imaging systems, contrast is the result of the difference in the reflectivity (scattering) and orientation of the object. In passive imaging systems, contrast is the result of temperature and radiation difference of the object. Passive systems, while not exhibiting the large dynamic range of active counterparts, are inherently multimode which, to some degree, slightly compensates for their smaller dynamic range. This paper overviews the latest developments of image sensor architectures which can potentially be utilized in active or passive imaging systems.

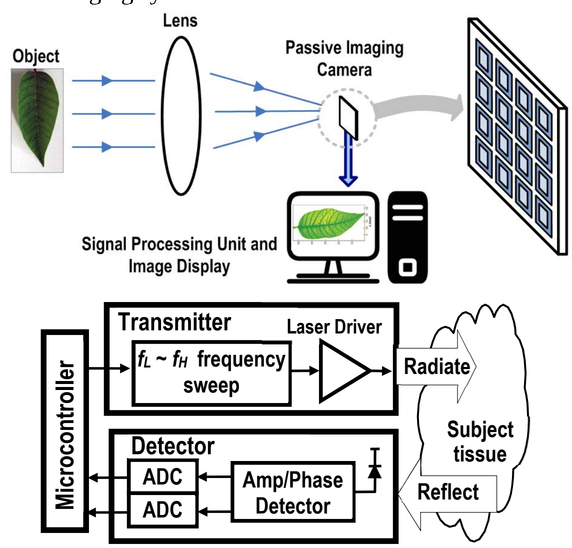

Fig. 4. (a) Focal-plane array (FPA) imaging sensor, and (b) optical-based active imaging sensor.

A. mm-Wave/THz Passive Imaging Sensors

A passive imaging sensor is primarily a detector (or array of detectors) with great sensitivity (Fig. 5(a)).

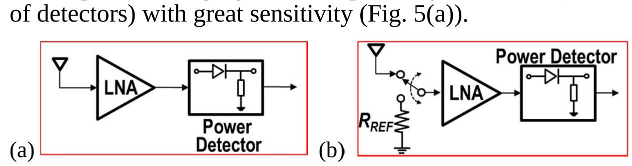

Fig. 5. (a) A simple director-detection-based passive imaging sensor. (b) A Dicke-based passive imaging sensor.

The sensitivity is characterized by noise equivalent temperature difference (*NETD*). The *NETD* measures the minimum temperature change from the scene's nominal temperature that results in detectable rms voltage change at the output of the sensor. The *NETD* is given by (2) [7-12]:

$$NETD=\sqrt{\frac{T_{SYS}^2}{BW.\tau}+T_{SYS}^2\left(\frac{\Delta G}{G}\right)^2+\frac{1}{2\tau}.\left(\frac{NEP}{k_B.G.BW}\right)^2} \qquad (2)$$

where T_{SYS} is the system noise temperature, *BW* denotes the bandwidth, τ is the back-end integration time, *G* is the pre-detection gain, ΔG is the rms variation of *G*, and *NEP* represents the noise equivalent power of the receiver [7-12]. ΔG is often the dominant term in (2), and can degrade the *NETD* significantly. For a stand-alone detector acting as a simple imaging RX without any pre-amplification, the *NEP* rather than noise figure (*NF*) is the proper measure for noise performance, because a square-law detector is essentially a non-linear circuit measuring the input power and producing a DC voltage. For a direct-detection-based imaging RX in Fig. 5(a), consisting of a gain stage (e.g., LNA) and a power detector [9-11], both the noise temperature (or *NF*) of the gain stage and noise from the detector (measured by *NEP*) contribute to overall system noise. Therefore, the system *NETD* is obtained by superposing the noise contribution from the pre-amplification stage and the detector using (2).

A.1 Dicke-Based Passive Imaging Sensors

The gain fluctuation problem is alleviated by periodically chopping the received signal above the gain fluctuation frequency using a front-end switch, that switches periodically between antenna and a reference resistor [12] (see Fig. 5(b)). In addition to the gain fluctuation problem, 1/f noise is considered to be another source of low frequency disturbance, affecting the system *NETD* in a similar way. The chopping frequency, therefore, needs to be higher than the 1/f noise corner frequency. Typically, the Dicke switch is implemented as an SPDT switch using PIN diodes [12]. The SPDT switch in silicon technologies exhibits considerable loss. Fig. 6 exhibits the receiver *NETD* due to the SPDT loss. 5-dB switch insertion loss in SiGe BiCMOS process results in 3K *NETD*, significantly worse than that of an Indium-Phosphide (InP) PIN diode-based switch.

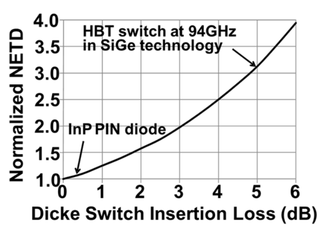

Fig. 6. The normalized *NETD* vs. insertion loss of the SPDT switch.

To mitigate the large insertion loss of SPDT switches implemented in silicon process, [10] proposed a direct-detection-based passive imaging sensor, shown in Fig. 7(a), that utilized a new balanced LNA with embedded Dicke switch. Inspired by a GaAs implementation [14], the architecture is comprised of a balanced LNA with the addition of a reflection-type binary phase shifter (RTPS) in each branch (Fig. 7(b)). When the phase shifters are in the same state (S1 off - S2 off or S1 on - S2 on), the circuit reduces to a standard balanced LNA, and the amplified signal from the antenna input appears at the output port. However, when the phase shifters are in opposite states (S1 off - S2 on or S1 on - S2 off), there is an extra 180° phase shift in the reference branch. This results in a constructive amplification of the noise power from the 50-Ω reference input, while the signal from the antenna input is suppressed. By toggling between these two states, the desired chopping operation of the Dicke switch is achieved. System analysis shows that implementing the Dicke switch functionality using this architecture yields a 2.5-dB improvement in the *NF* of the front-end amplifier and 2× improvement in *NETD*.

A mechanical drawing of the imaging test setup is shown in Fig. 8(a). A 12-18-GHz signal generator drives a ×6 multiplier, providing a transmit power of -30 dBm at 90 GHz to a WR-10 horn antenna. The radiated power from the antenna illuminates the object of interest, which, in turn, increases the SNR at the RX input. Fig. 8(b) shows the lab setup for the line-of-sight active measurement of the passive imaging RX. A simple MMW image of an envelope containing a coin was created and demonstrated in Fig. 8(c). The image was generated one pixel at a time, by stepping the envelope position over a 60×40mm^2 area in 5-mm increments. This coarse step was chosen due to the limited accuracy of manual movement of the envelope. The chip output voltage was read on an oscilloscope for each pixel. The receiver chip achieved a measured responsivity of 20-43 MV/W with a front-end 3-dB bandwidth of 26 GHz, while consuming 200 mW of power. The calculated *NETD* of the SiGe receiver chip is 0.4K with a 30 ms integration time.

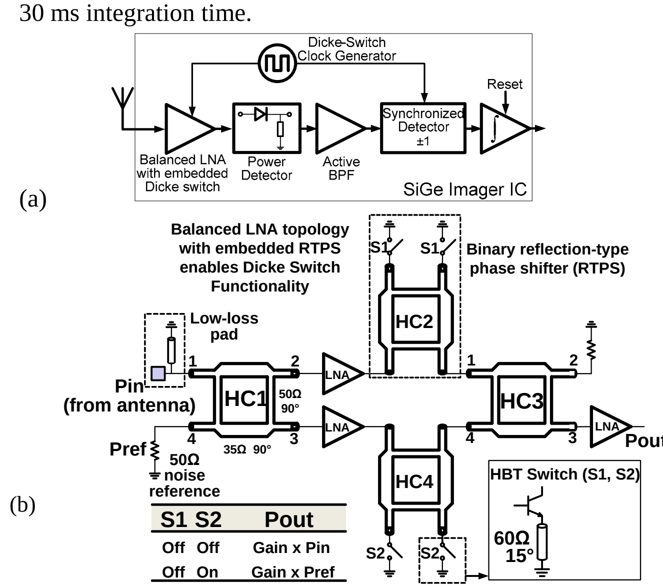

Fig. 7. (a) A passive imaging sensor incorporating a balanced LNA with embedded Dicke switch. (b) The circuit schematic [10].

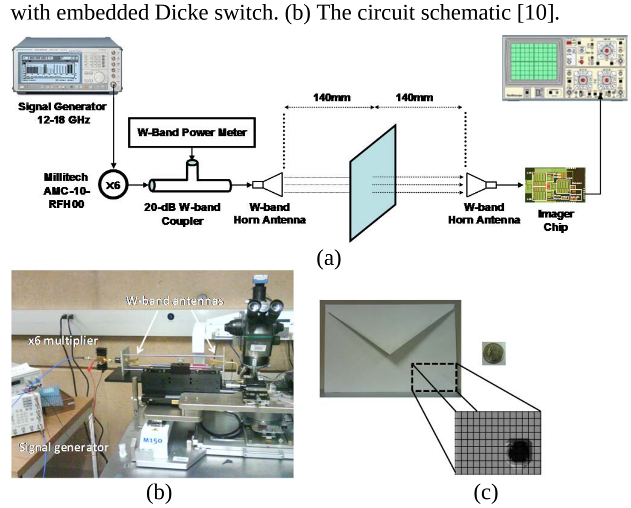

Fig. 8. (a) block diagram of the test setup. (b) A view of the lab setup, and (c) the image of the coin hidden inside an envelope [10].

A.2 Focal-Plane Array Imaging Sensors with Spatially Overlapping Super-Pixels

A conventional focal plane array (FPA) sensor is realized as an $M \times N$ array of elements. Shown in Fig. 9 is an example of a 2×2 FPA, where each element, A_k, feeds one detector, D_k, representing one pixel of an image.

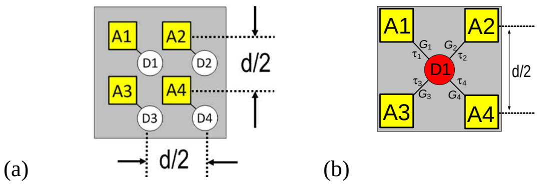

Fig. 9. (a) A conventional 2×2 FPA, and (b) a 2×2 sub-array feeding one detector.

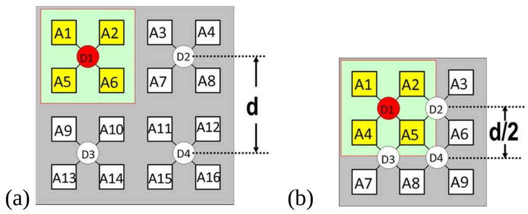

Fig. 10. (a) Conventional array of non-overlapping subarrays and (b) New array of overlapping super-pixels [17].

Alternatively, a 2×2 array of elements feeding one detector and forming one pixel is depicted in Fig. 9(b). If delay and amplitude control mechanisms (G_k and τ_k in Fig. 9(b)) are incorporated in the RF-path of each element to detector, then this 2×2 array realizes a "super-pixel" [17]. These delay/gain weightings enable the super-pixel to constrict the field of view of the feed antenna so that more energy illuminates the lens and less is lost to spillover, with a resulting SNR improvement dependent upon the original spillover losses.

A straightforward way of aligning super-pixels within a larger array is to place each super-pixel such that the element-to-element spacing of adjacent super-pixels remains at $d/2$, as shown in Fig. 10(a). In this case, although the element spacing remains the same when compared to a traditional array, the pixel spacing is increased resulting in a physically larger array for the same number of pixels. While the optics can be chosen to match this array design, the increased physical size of the array would be an undesirable overhead.

A "hybrid" architecture is discovered to take advantage of the traditional focal plane array pixel spacing and the super-pixel capability [17]. In this architecture (Fig. 10 (b)), the super-pixels overlap and share neighboring elements, and hence, are referred to as spatial-overlapping super-pixels. Each detector is still fed by four elements as in a conventional array of super-pixels, but each element now feeds up to four detectors depending on the element's location within the array (Fig. 10(b)).

The use of spatial-overlapping super-pixels results in (1) improved SNR at the pixel level through a reduction of spillover losses, (2) partially correlated adjacent super-pixels, (3) a 2×2 window averaging function in the RF domain, (4) the ability to compensate for the systematic phase delay and amplitude variations due to the off-focal-point effect for antennas away from the focal point, and (5) the ability to compensate for mutual coupling among the array elements. A 3-D view of a complete super-pixel circuit is shown in Fig. 11. The proposed 3×3-element array was fabricated in a SiGe BiCMOS process. An *NETD* of 0.45K was directly measured with the hot/cold test setup, which is the lowest *NETD* reported for any silicon-based fully integrated imaging sensor.

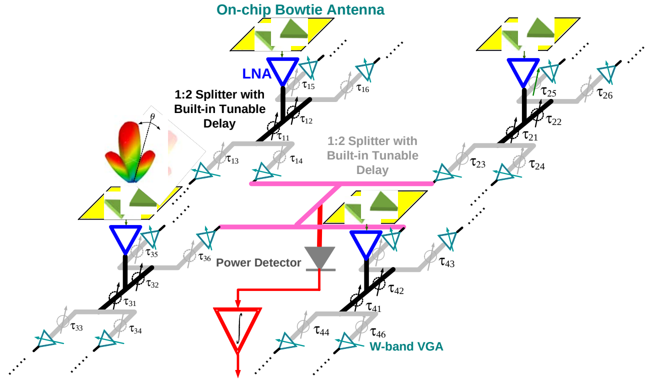

Fig. 11. 3-D view of a 2×2 super-pixel [17].

Fig. 12 shows the setup used to construct the image of objects. In this setup, the illumination frequency was 90 GHz, the output power of the illuminating source was set to a level to prevent saturation of the integrator, the integration time was 20ms, the distance from the illuminating source to the object was 20cm, and the object-to-receiver distance was 30cm. The receiver chip was programmed to 0° beam steering with maximum gain. The object was then stepped in the x and y directions in 4mm increments and the detector outputs were recorded 10 times at each position and then averaged. The total scan time was greater than one hour due to the manual operation of the stepper.

Fig. 13 shows the images from the outputs of four individual super-pixels, obtained by 4mm spatial sampling, compared with the image obtained by combining the four overlapping super-pixels' data, resulting in 2mm sampling. It can be visibly seen that the 2mm over-sampled image results in a sharper spatial resolution.

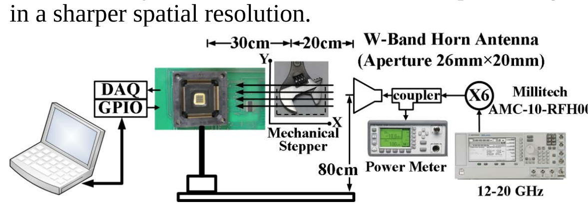

Fig. 12. Test setup to form image of objects using the 9-element imaging array sensor [17].

Fig. 13. Reconstructed images from the outputs of four individual 2×2 subarrays, along with the composite image obtained by combining the four overlapping subarray images [17].

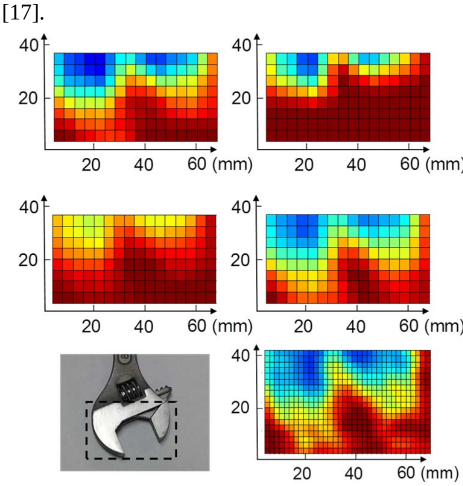

The receiver chip achieves a peak measured coherent responsivity of 1,150MV/W, a measured incoherent responsivity of 1,000MV/W and a front-end 3-dB bandwidth from 87-108GHz, while consuming 225mW per receiver element. The measured *NETD* of the SiGe receiver chip is 0.45K with a 20ms integration time.

B. mm-Wave/THz Active Imaging Sensors

A widely known example of an active imaging sensor is a radar. Radars primarily detect and track objects, and provide a highly accurate measurement of the distance, velocity and direction of the detected objects. In principle, every radar system (a) transmits electromagnetic energy to search for objects in a specific volume in space, (b) detects the energy reflected from objects in that volume, (c) measures the time between the two events, and (d) ultimately provides estimates of range, amplitude and velocity of the objects based on the detected energy and measured time. Several other conventional systems, including infrared and video sensors, have typically been used to perform the above functions, but radars have a significant advantage of being highly immune to environmental and weather conditions.

Fig. 14 demonstrates the operation principle of an FMCW radar, which is the underlying system architecture for the continuous-wave (CW) terahertz spectroscopy. There are two frequency shifts in the returned echo signal that add up to a total shift, i.e., f_τ frequency shift due to running time (target range) and f_D frequency shift due to Doppler frequency (target radial velocity). Two variables are resolved in the frequency-chirped radars, namely the range and the Doppler Effect. One problem with frequency-chirped radar is that the resolution is related to how fast and over how wide a bandwidth is possible to generate a well-defined chirp. Close-range and closely spaced targets also put stringent requirements on the phase noise. This notion suggests the use of closed-loop frequency synthesizer rather than an open-loop oscillator to generate the frequency chirps.

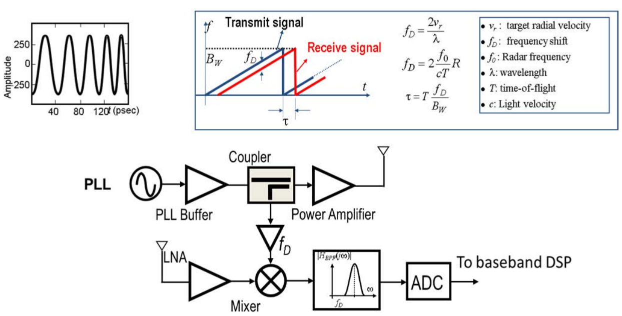

Fig. 14. Operation principle of an FMCW radar.

In fact, open-loop signal sources exhibit severe frequency fluctuation, and are vulnerable to temperature/process/supply induced frequency drift. This is especially critical for THz sensing systems such as FMCW radars. The need for stable/precise oscillation frequency with wide tuning range and low close-in phase noise calls for closed-loop source topologies. MMW PLLs incorporating push-push VCOs have been demonstrated up to 164GHz in silicon technologies [18]. [19] presented a 300GHz PLL with 0.12% locking range in III-IV technology.

In a high frequency synthesizer (FS), the VCO and the divider both exert dominant effects on the locking range, phase noise, and output power. Starting with the VCO, achieving wide tuning range, low phase noise, and high output power simultaneously is challenging. This is because of the limited f_T/f_{max} of transistors and low Q factor of varactors at high frequencies in silicon. The output power degrades more severely in harmonic VCOs, as the varactor loss is much higher at harmonic frequencies. Furthermore, the first stage divider in a PLL suffers from low frequency range and high DC power dissipation. To alleviate these problems, a THz phase-locked-based synthesizer should incorporate three novel techniques [20]: (1) optimum signal condition (OSC) methodology, (2) Colpitts-based active varactor (CAV), and (3) VCO/divider co-design.

When VCO is employed in a PLL, additional concerns arise. One important issue at high frequencies is the connection between the VCO and the first frequency divider. The VCO, which is already under stringent requirements, has to provide strong signals to the divider. As an injection locked divider its locking range is a strong function of its input power. This results in another tradeoff in the VCO/divider design. More power transfer from the VCO to the divider results in higher locking range of the divider. This comes at the expense of a decrease in the swing of the VCO's fundamental frequency, and hence, a decrease in the harmonic output power.

To overcome these challenges, we introduce a new block called Colpitts-based active varactor (CAV) [20]. The CAV has three important roles: (1) It provides a wide tuning range variable capacitor with almost no loss to the VCO for frequency tunability; (2) It isolates the varactor and its loss from the VCO to increase the fundamental frequency (f_o) voltage swing and harmonic power; and (3) It buffers the f_o signal and injects it to the divider without loading the oscillator.

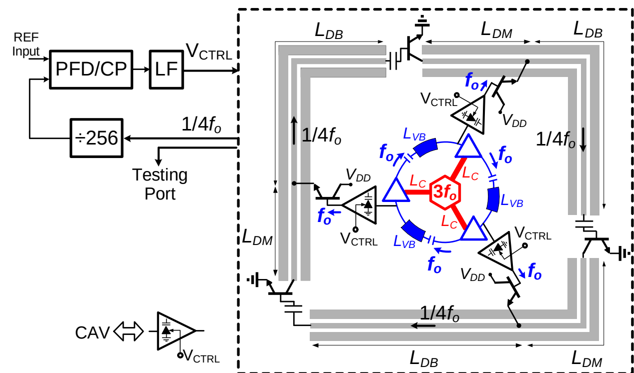

Fig. 15. Block diagram of a THz PLL-based synthesizer [20].

At high frequencies, any interconnect or cross-over introduces parasitics that cause severe signal distortion. This distortion will adversely affect the performance of the synthesizer's VCO and divider such as phase-noise, output power, and input sensitivity. The structural similarity of the proposed VCO and the three-phase injection divider helps us co-design/co-optimize these blocks and develop a compact layout. Shown in Fig. 15 are system block diagram of a THz frequency synthesizer and integration of the VCO and the divider within the synthesizer, where the inner blue circle indicates the VCO ring. The VCO's f_o travels along the inner blue ring and its 3rd harmonic signals are collected coherently at the center's $3f_o$ pad. The t-line's length realizing L_C determines the perimeter of the VCO ring and the length of L_{VB}. The t-line L_{VB}, used to introduce 10-degree phase shift for transistor optimum condition, forms the ring's perimeter. By narrowing L_C and widening L_{VB} to proper values, the L_{VB}'s t-line is fitted into the VCO ring. Three CAVs are placed in the layout with respect to divider's three-phase inputs such that no extra t-line or signal cross-over is required. The outer rectangle realizes the divider's loop, which is locked to the VCO ring and performs divide-by-4. The divider's output $1/4f_o$ is then fed to the divide-by-256 and forms a close-loop through PFD/CP and LF.

Shown in Fig. 16 is the measurement of the synthesizer's scale-up phase-noise versus its output frequency. The locking range varies from 280~303 GHz (i.e., 7.9% tuning range), thereby closely following the VCO's tuning range. The minimum phase-noise at 1 MHz offset is -75.4 dBc/Hz when the synthesizer's output frequency is 296 GHz. With the input signal fed from a 96 MHz crystal oscillator (i.e., the synthesizer's output frequency is 294.9 GHz), the measured phase-noise is -82.5 dBc/Hz (-89.6 dBc/Hz) at 1 MHz (10 MHz) offset [20]. The overall power dissipation of this THz synthesizer is 376 mW.

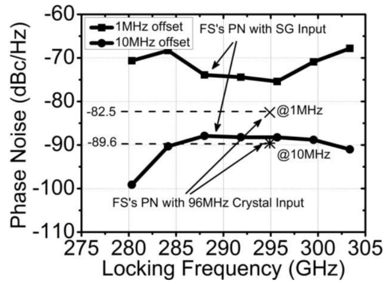

Fig. 16. The measurement of the synthesizer's scale-up phase-noise versus its output frequency with the synthesizer's input reference from a SG and a crystal oscillator [20].

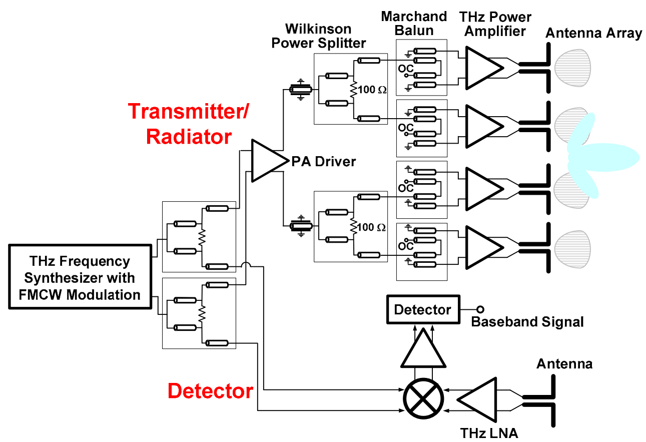

Fig. 17. A THz FMCW active radar with spatial power-combining capability.

The high integration density of silicon technologies makes it possible to design sophisticated active imaging sensors that employ multi-antenna architectures. The use of multi-antenna TRX's brings forth two essential features; namely spatial power combining and electrical beam-steering. These two features help enhance the scanning time of the object and increase the radiation power and thus penetration depth. Fig. 17 shows an example of a multi-antenna THz active imaging sensor that uses FMCW modulation to capture Doppler effect. The radiator side uses a THz power distribution network that allows the FMCW signal to be effectively guided to four power amplifiers and antenna elements, thereby allowing the beam-narrowing and spatial power combining. The RX side incorporates a correlation-based architecture where the received signal is compared against the template generated by the THz synthesizer. Upon maximum correlation the signal is detected and reconstructed in the baseband.

III. CONCLUSION

Aggressive feature-size scaling in CMOS technologies, readily resulting in scaling of f_T/f_{max} to sub-THz frequencies, allows designing very high performance THz imaging sensors for near-field IoT. This paper gave an overview of advances in silicon-based integrated circuits design enabling mm-wave/THz passive/active imaging sensors. Several system-level considerations and circuit design issues were discussed and case studies were presented.

ACKNOWLEDGEMENT

The author thanks all former Ph.D./post-doc students at the NCIC Labs, in particular, Dr. Zheng Wang, Dr. Pei-Yuan Chiang, Dr. Francis Caster, II, Dr. Leland Gilreath, and Prof. Omeed Momeni. He also acknowledges TowerJazz Semiconductor for fabricating the integrated circuits discussed in this paper. This research was funded in part by grants from NSF ECCS-1408547 and Samsung Advanced Institute of Technology.

REFERENCES

[1] https://internetofthings.ibmcloud.com/#/
[2] http://www.uni-konstanz.de/FuF/Physik/terahertz/research.htm
[3] D. L. Woolard et al., "Submillimeter-wave phonon modes in DNA macromolecules," *Phys. Rev. E*, vol. 65, pp. 1903–1914, 2002.
[4] T. R. Globus *et al.*, "THz spectroscopy of biological molecules," *J. Biol. Phys*., vol. 29, pp. 89–100, 2003.
[5] D. L. Woolard et al., "Terahertz Frequency Sensing and Imaging: A Time of Reckoning Future Applications?" *Proc. of IEEE*, vol. 93, no. 10, pp. 1722 – 1743, Oct. 2005
[6] http://www.lakeshore.com/products/THz-System/Pages/technology.aspx
[7] J. W. May and G. M. Rebeiz, "Design and Characterization of W-Band SiGe RFICs for Passive Millimeter-Wave Imaging," *IEEE Trans. Microwave Theory Tech*., vol. 58, no. 5, pp. 1420-1430, May 2010.
[8] A. Tomkins, P. Garcia, and S. P. Voinigescu, "A passive W-band imager in 65nm bulk CMOS," *IEEE CSICS*, pp. 1-4, Oct. 2009.
[9] L. Zhou, et al., "A W-band CMOS Receiver Chipset for Millimeter-Wave Radiometer Systems," *IEEE J. Solid-State Circuits*, vol. 46, no. 2, pp. 378-391, Feb. 2011.
[10] L. Gilreath, V. Jain, and P. Heydari, "Design and Analysis of a W-Band SiGe Direct-Detection-Based Passive Imaging Receiver," *IEEE J. Solid-State Circuits*, vol. 46, no. 10, pp. 2240-2252, Oct. 2011.
[11] Z. Chen, et al., "A BiCMOS W-Band 2×2 Focal-Plane Array with On-chip Antenna," *IEEE J. Solid-State Circuits*, vol. 47, no. 10, Oct. 2012.
[12] J. J. Lynch, et al., "Passive millimeter-wave imaging module with preamplified zero-bias detection," *IEEE Trans. Microwave Theory Tech.*, vol. 56, no. 7, pp. 1592–1600, July 2008.
[13] C. Martin, et al., "Rapid passive MMW security screening portal," *Proceedings of SPIE Defense and Security 2008*, vol. 6948.
[14] D.C.W. Lo, et al., "A monolithic W-band high gain LNA/Detector for millimeter-wave radiometric imaging applications," *IEEE MTT-S International Symposium*, pp. 1117-1120, June 1995.
[15] M. Planck, *The Theory of Heat Radiation*. Masius, M. (transl.) (2nd ed.), 1914
[16] http://ozonedepletiontheory.info/follow-the-energy.html
[17] F. Caster, II, L. Gilreath, S. Pan, Z. Wang, F. Capolino, and P. Heydari, "Design and Analysis of a W-band BiCMOS9-Element Imaging Array Receiver Using Spatial-Overlapping Super-Pixels," *IEEE J. Solid-State Circuits*, vol. 49, no. 6, pp. 1317-1332, June 2014.
[18] S. Shahramian, *et al.*, "Design of a dual W- and D-band PLL," *J. Solid-State Circuits*, vol. 46, no. 5, pp. 1011–1022, May 2011.
[19] M. Seo *et al*., "A 300 GHz PLL in an InP HBT Technology," *IEEE MTT-S Int. Microw. Symp. Dig*., pp. 1–4, June 2011.
[20] P.-Y. Chiang, Z. Wang, O. Momeni, and P. Heydari, "A Silicon-Based THz Frequency Synthesizer with Wide Locking Range,"*IEEE J. Solid-State Circuits*, vol. 49, no. 12, pp. 2951-2963, Dec. 2014.